ZnO Hard Templating for Synthesis of Hierarchical Porous Carbons with Tailored Porosity and High Performance in Lithium-Sulfur Battery

*Patrick Strubel, Sören Thieme, Tim Biemelt, Alexandra Helmer, Martin Oschatz, Jan Brückner, Holger Althues, and Stefan Kaskel**

Hierarchical porous carbon (HPC, DUT-106) with tailored pore structure is synthesized using a versatile approach based on ZnO nanoparticles avoiding limitations present in conventional silica hard templating approaches. The benefit of the process presented here is the removal of all pore building components by pyrolysis of the ZnO/carbon composite without any need for either toxic/reactive gases or purification of the as-prepared hierarchical porous carbon. The carbothermal reduction process is accompanied by an advantageous growing of distinctive micropores within the thin carbon walls. The resulting materials show not only high internal porosity (total pore volume up to 3.9 cm^3 g^{-1}) but also a large number of electrochemical reaction sites due to their remarkably high specific surface area (up to 3060 m^2 g^{-1}), which renders them particularly suitable for the application as sulfur host material. Applied in the lithium-sulfur battery, the HPC/sulfur composite exhibits a capacity of >1200 mAh g^{-1}-sulfur (>750 mAh g^{-1} electrode) at a high sulfur loading of ≥ 3 mg cm^{-2} as well as outstanding rate capability. In fact, this impressive performance is achieved even using a low amount of electrolyte (6.8 µl mg$^{-1}_{\text{sulfur}}$) allowing for further weight reduction and maintenance of high energy density on cell level.

1. Introduction

The increasing demand for portable energy storage devices requires new systems with high energy density, improved safety, long-term durability, and in particular the use of low-cost materials.[1–3] One of the most promising candidates for these next generation systems is the lithium-sulfur (Li-S) battery. Sulfur offers the highest theoretical capacity of all known solid-state cathode materials (1672 mAh g$^{-1}_{\text{sulfur}}$) and is widely abundant in nature, inexpensive as well as environmentally friendly. These factors highlight the attractiveness of Li-S batteries for wide-range power supply.

However, despite more than two decades of intensive scientific research focusing on all cell components, the wide market penetration of a viable Li-S battery has not been realized so far. This is caused by several challenges coupled with the complicated electrochemical conversion of sulfur in liquid organic electrolytes. Major drawbacks are the repeated dissolution and deposition of highly insulating sulfur compounds and the extensive expansion and shrinking of the active material (mechanical degradation of the cathode structure) during cycling.[4–6] Moreover, the Coulombic efficiency of the Li-S cell is largely decreased by a parasitic self-discharge mechanism referred to as polysulfide shuttle.[7]

On the cathode side, a tailored conducting sulfur host structure is required due to the electrically insulating character of the active material species (S_8, Li_2S_2/Li_2S). Up to date, large numbers of novel, elaborate host structures have been explored, such as porous carbons,[8–12] (reduced) graphene oxide[13,14] and carbon nanotubes (CNTs).[15–19] Porous carbons tend to be the ideal matrix due to their low weight, high conductivity as well as adjustable structural properties, including the pore volume, pore size and specific surface area. Major improvements were achieved by employing advanced porous carbon materials with high surface area as well as nanostructured pore systems for that purpose.[20] However, several important requirements coupled with the cell characteristics of Li-S systems have to be considered for these materials. To obtain high energy densities in such a device, not only a high sulfur loading but also a high active material utilization is crucial. In addition, electrolyte wetting of the electrode and the compensation of the volume expansion during discharge play an important role as well. Therefore, it is a key issue to design a nanostructured porous carbon material with pore properties especially tailored for the application in high capacity Li-S batteries. Commercially available microporous carbons (pore size <2 nm) are not very attractive due to their low pore volume limiting the achievable sulfur content. The pioneering work of Nazar and co-workers[8] illustrated the advantages of using ordered mesoporous CMK-3 as a conductive framework with

P. Strubel, S. Thieme, A. Helmer, J. Brückner,
Dr. H. Althues, Prof. S. Kaskel
Fraunhofer Institute for Material and Beam Technology
Winterbergstraße 28, D-01277 Dresden, Germany
E-mail: stefan.kaskel@chemie.tu-dresden.de
T. Biemelt, M. Oschatz, Prof. S. Kaskel
Department of Inorganic Chemistry
Dresden University of Technology
Bergstraße 66, D-01062 Dresden, Germany

DOI: 10.1002/adfm.201402768

highly accessible nanopores. Further investigations were performed by Li et al.[21] showing that capacity fading was not significantly increased for larger mesopore (2 nm < pore size < 50 nm) sizes. Nevertheless, permanent capacity loss was observed even after several formation cycles, which is indicative for a continuous precipitation of insulating Li_2S-particles outside the electrically conductive carbon matrix leading to loss of contact. Hence, it was concluded that the mere increase of pore volume achieved by adjusting larger pore diameters is still insufficient for long-term capacity retention. Studies of Liang et al.[22] revealed that it is beneficial to introduce additional microporosity in a mesoporous carbon, since the resulting higher specific surface area (SSA) boosts the active material utilization and decreases the capacity loss. In recent years many novel hierarchical porous carbon materials with good performance in Li-S cells have been reported illustrating the synergetic advantage of a bimodal porosity.[9,22–27] However, the production schemes of such highly optimized sulfur host structures are often complicated. Since scalability of material production plays a crucial role for the final success of one approach over another, special attention needs to be drawn to the development of suitable and effective production processes. In most cases hierarchical porous carbons with the above-mentioned porosity are produced following a complex two-step route. First, the meso/macroporous carbon is synthesized by a nanocasting approach mostly using of silica particles as hard template followed by physical or chemical activation generating the required additional micropores. However, low carbon yield, and process issues, which are the consequence of a time consuming wet silica etching process (template removal) as well as further purification steps lead to economic and ecologic drawbacks. More favorable soft templating approaches, developed by Zhao and co-workers[28] as well as recently published "salt templating" approaches[29] are impressive. Nevertheless, the process does not support the tailoring of pore sizes in a wide range and the purification step is still inevitable. Thus, new hard templates need to be identified, which bear down the current deficits caused by the application of silica particles.

Here, we present the synthesis of hierarchical porous carbons by using inexpensive, commercially available zinc oxide nanoparticles as hard template, which is a scalable and efficient alternative route overcoming the limitations mentioned. One major benefit of the process is the in situ removal of all pore building components through carbonization. Thus, no toxic/reactive gases are required in the process and purification of the as-prepared porous carbon is not necessary. The obtained carbon material provides a high internal porosity (total pore volume up to 3.9 $cm^3\ g^{-1}$) and a large number of electrochemical reaction sites due to its high specific surface area (up to 3060 $m^2\ g^{-1}$). When applied as cathode with high sulfur loading (≥3 $mg_{sulfur}\ cm^{-2}$) in the Li-S cell, the melt-infiltrated carbon (carbon/sulfur composite) exhibits a capacity of more than 1200 mAh $g^{-1}{}_{sulfur}$ (>750 mAh $g^{-1}{}_{electrode}$).

2. Results and Discussion

2.1. Synthesis of Hierarchical Porous Carbon

The synthesis of hierarchical porous carbons (HPC) with well-defined and tailored porosity using zinc oxide nanoparticles (ZnO-NP) as hard template has not been described so far. ZnO-NP are an inexpensive mass product, non-toxic, and exhibit interesting chemical properties rendering them a highly attractive material for hard templating approaches.[30,31] For instance, in contrast to established silica particles, the ZnO-NP template can be removed through dissolution in moderate acids or even more favorable through carbothermal reduction according to the following reaction.

$$\mathrm{ZnO} + x\mathrm{C} \rightarrow \mathrm{Zn} + (x-1)\mathrm{C} + \mathrm{CO} \qquad (1)$$

Pyrolysis temperatures above the boiling point of zinc ensure the synthesis of porous carbons with highly efficient and constructive in situ template removal without any need for toxic or reactive gases. The hard template approach was realized as shown in the process scheme in **Figure 1**. In the first step, the nanoparticles were encapsulated by sucrose as the carbon precursor. This hydrocarbon is particularly suitable for the preparation of meso/macro porous carbons with microporosity inside the carbon walls due to the in situ micropore growing during pyrolysis.[32] In addition, sucrose can be converted into carbon with a high atom efficiency (42 wt%), which is beneficial for the reaction yield. The hierarchical porous carbon is obtained by subsequent pyrolysis and hard template removal (carbothermal reduction) under inert gas flow without further purification.

The controlled decomposition of sucrose in aqueous solution, which is usually promoted by an acid catalyst (low pH value), is a crucial step to form a homogenous carbon layer on the ZnO surface being required for a well-defined hard template replication. However, ZnO-NP are not inert under acidic and basic conditions, but rather react to numerous different ionic species depending on pH value.[33] Nevertheless, surface charge and thus, the zeta potential, can be influenced. This not only improves the dispersibility of large nanoparticle aggregates but also prevents the agglomeration of the nanoparticles

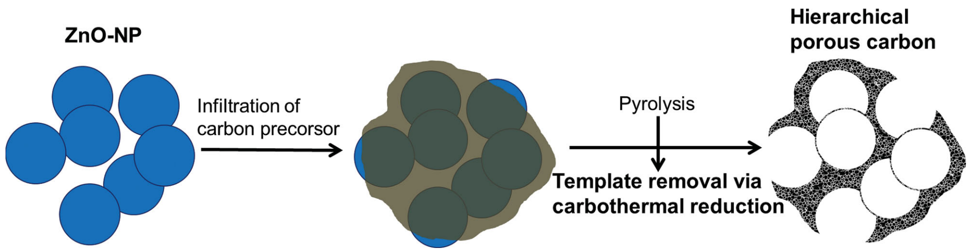

Figure 1. Schematic of the hierarchical porous carbon synthesis.

during sucrose decomposition. Thermogravimetric analyses were performed to investigate the impact of the pH value of the sucrose solution (Figure S1, Supporting Information). All curves show the same trend with two significant weight loss steps. The first step can be attributed to the pyrolysis of sucrose at 200 °C to 500 °C corresponding to its carbonization, while the second step above 800 °C is indicative for the carbothermal reduction of ZnO. These results indicate a strong influence of pH value on the template approach. Shifting the pH value to basic conditions decreases the temperature until the carbothermal reduction is finished. It is believed that the basic pH value supports the desirable interaction between sucrose and ZnO surface. Therefore, an apparently more homogenous distribution of ZnO-NP in the templating step can be obtained resulting in a thinner carbon film on the nanoparticle surface. The more intimate contact between carbon precursor and ZnO template might lead to faster reaction kinetics during carbothermal reduction, thus reducing the activation energy and consequently the reaction temperature.

2.2. Characterization of Hierarchical Porous Carbon

To illustrate the versatility of the synthesis approach, three different ZnO-NP templates were investigated. TEM images of the purchased nanoparticles (Figure S2a,b) show spherically shaped particles with relatively broad size distribution in range of 10 to 100 nm, especially for the Evonik Industries (EI) particles. In contrast, the nanoparticles derived from US-Nano (USN) show larger particle size mainly above 50 nm. A monomodal particle size of approximately 20 nm is only observed for the ZnO-NP synthesized in house (self-made, SM).

2.2.1. Influence of Carbothermal Reduction

The selective removal of the template is a crucial step in the synthesis of a porous carbon material with high pore volume. According to the mentioned TG investigations (Figure S1), the carbothermal reduction can be considerably controlled by adjusting the pyrolysis temperature (Figure S3, Supporting Information). At 950 °C a complete removal of ZnO is possible during the pyrolysis step, whereas at 800 °C ZnO residues [ICDD: 36-1451] remain inside the carbon material as is evidenced by the corresponding XRD pattern (Figure S3a,b). Surprisingly the reactivity of a ZnO/sucrose (2:1, m:m) sample prepared from basic sucrose solution (ZnO-b) was found to be much higher than the reactivity of the corresponding sample prepared from acidic (ZnO-a) solution. This led to the complete consumption (oxidation) of the carbon precursor (through carbothermal reduction of ZnO) already at 800 °C under basic catalytic conditions, whereas no substantial carbon loss was observed under acidic conditions (Figure S4). It is assumed that the different behavior arises from the closer contact between carbon and zinc oxide in the C/ZnO-b composite.

To remove the ZnO residues from C/ZnO-a after pyrolysis at 800 °C the sample was washed with diluted HCl. In order to achieve an eligible comparison, the amount (molar equivalent) of carbon theoretically consumed by the carbothermal reduction was added beforehand by increasing the sucrose-to-ZnO ratio. In the following all carbothermally reduced carbons are named HPCR (hierarchical porous carbon – carbothermally reduced), whereas all HCl-washed samples are named HPCW (hierarchical porous carbon – washed). The nitrogen physisorption isotherms measured at –196 °C (**Figure 2**a) show a considerable nitrogen uptake at both low ($p/p_0 < 0.1$) and high ($p/p_0 > 0.8$) relative pressure. However, the curve of a typical HPCR sample show, in direct comparison to HPCW, an impressive increase of the adsorbed nitrogen volume at low relative pressure indicating that the specific surface area is remarkably higher. In fact, the surface area calculated by multi-point BET analysis for the HPCR sample prepared from ZnO-NP purchased from US-Nano (HPCR-USN) exceeds 1700 $m^2 g^{-1}$ (**Table 1**), which is more than twice the surface area of HPCW prepared from the same template (HPCW-USN).

In the range of $0.1 < p/p_0 < 0.8$ neither a significant adsorption nor a distinctive hysteresis loop is observed evidencing the existence of a meso-macroporous system with micropores inside the carbon walls. SEM images (Figure S3c,d) show the presence of a highly connected porous network inside a large carbon particle with predominantly spherically shaped pores smaller than 100 nm. HPCW-USN, however, feature larger interconnected pores as well. This may be due to the aggregation of ZnO-NP during synthesis process as supposed for HPC prepared from ZnO-a. In consideration of the harsh synthesis conditions during the carbothermal reduction step: 1) high temperature of 950 °C, 2) gradual reduction of ZnO template under consumption of carbon atoms located in the thin carbon layer surrounding the ZnO-NP (pore walls), 3) evaporation of elemental zinc and diffusion of zinc vapor through the carbon particle; it is very impressive that a highly porous structure with thin and unbroken carbon walls can be obtained (Figure 2c). A high-magnification TEM image further shows that the carbon walls of the HPCR are smaller than 5 nm in thickness and predominantly consist of disordered sp^2 carbon fringes (Figure 2d). Due to the large uptake of nitrogen at high relative pressure the quantitative analysis of both, total pore volume and complete pore size distribution is not possible only from nitrogen physisorption measurement. Therefore, mercury intrusion analysis was performed to investigate the overall porosity. The mercury intrusion curves of characteristic samples of HPCW-USN and HPCR-USN, respectively, (Figure S5, blue and black curve) show a two-step intrusion indicating pores of large as well as small diameter. The first step corresponds to the quasi-pores generated by the void space between the loosely packed, large HPC particles. Thus, they do not contribute to the internal pore volume. The second intrusion step at high pressure is related to the highly accessible, hierarchical pore system inside the single particles. HPCR-USN possess a uniform distribution of small macropores of 70 nm in size with almost ideal replication of the ZnO-NP template (Figure 2b, for complete pore size distribution of all samples including quasi-pores see Figure S6) giving access to a new type of nanocasting approach. The procedure has the potential to substitute the conventionally applied, undesirable silica templates and, moreover, the versatile synthetic routes of different ZnO nanostructures ranging from spherical,[34] nanotubes,[35] tetrapods[36] as well as to porous ordered structures[37] should enable adjustable carbon pore

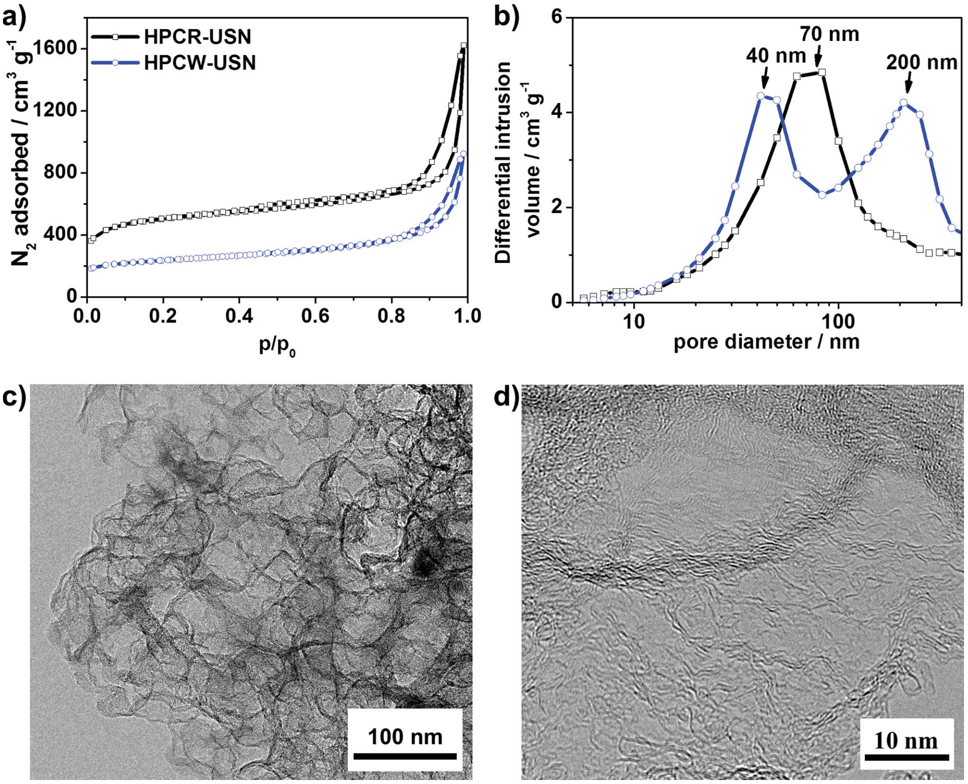

Figure 2. a) Nitrogen physisorption isotherms (–196°C) of HPCR-USN and HPCW-USN, respectively, b) corresponding mercury pore size distributions (5 nm to 400 nm), c,d) TEM images of HPCR-USN.

morphologies. In contrast, HPCW-USN shows a bimodal pore structure with pore maxima at 40 nm and 200 nm in accordance with SEM and TEM (Figure S3e) images. The total pore volume including the micropores as well as macropores with diameter ≤ 400 nm was calculated via a combination of nitrogen physisorption and mercury intrusion data and can be nearly as high as 4 cm^3 g^{-1} (Table 1) for both HPCR-USN and HPCW-USN. Accordingly, the pyrolysis temperature has no significant influence on the overall pore volume. The most impressive difference between the two samples is the considerable increase in micropore volume due to carbothermal reduction. A high value of 0.54 cm^3 g^{-1} is obtained, which is more than twice as high as the micropore volume achieved for the washed sample. This implies that the emission of gaseous CO_x species, which are formed in situ as a by-product of the carbothermal reduction process, can trigger the growth of micropores within the thin carbon walls. This is in principle analog to the well-known physical activation processes using CO_2 gas or steam. However, the significant advantage of the activation through carbothermal reduction over a post-synthetic activation is the formation of the reactive species inside the carbon particles. The micropores present in HPCW, in contrast, result from thermal decomposition of the hydrocarbon (sucrose) during pyrolysis.[32] Hence, the carbothermal reduction process facilitates the access of a distinctive hierarchical pore system with very high specific surface areas. Moreover, two essential process steps are integrated in the pyrolysis step of the presented approach: 1) in situ template removal due to consumption of the pore building ZnO-NP template; 2) introduction of micropores through an integrated CO_x activation.

2.2.2. Influence of ZnO Particle Size

The almost perfect template replication is a determining parameter of an advanced nanocasting route. It provides access to a precise tailoring of the properties of the resulting carbon replica and, in particular, allows the adjustment of the pore

Table 1. Influence of the ZnO removal technique on the porosity of HPC shown for samples synthesized from US-Nano ZnO-NP (USN).

Temperature of Pyrolysis	ZnO/Sucrose	Removal of ZnO-NP	Specific Surface Area [m^2 g^{-1}]	Total Pore Volume[a)] [cm^3 g^{-1}]	Micropore Volume[b)] [cm^3 g^{-1}]
800 °C	2/1	washing with diluted HCl	819	3.81	0.21
950 °C	2/1.75	carbothermal reduction	1757	3.69	0.54

[a)] calculated from the cumulated pore volume for pores with a diameter ≤ 400 nm using a combination of mercury intrusion data and nitrogen physisorption (micropore volume); [b)] calculated from the cumulated pore volume at a pore diameter of 2 nm using the QSDFT method.

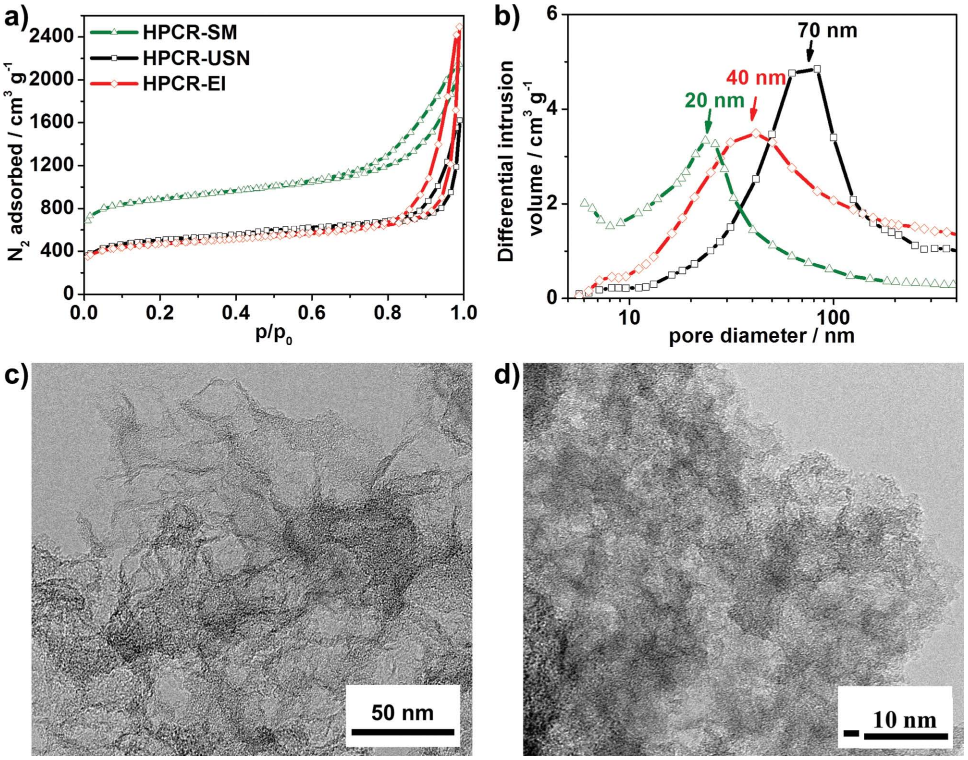

Figure 3. a) Nitrogen physisorption isotherms of HPCR prepared from different ZnO-NP, b) corresponding mercury pore size distributions (5 nm to 400 nm), c) TEM image of HPCR-EI, d) TEM image of HPCR-SM.

size. Nitrogen physisorption isotherms show significant differences depending on the ZnO-NP template used (**Figure 3**a). A decrease of nanoparticle size (Figure S2) shifts the hysteresis loop to lower relative pressure. The simultaneous change of nitrogen adsorption at low relative pressure ($p/p_0 < 0.1$) reflects the strong influence of the template particle surface area on the generation of micropores during carbothermal reduction. In particular, for the HPCR prepared from self-made ZnO-NP (HCPR-SM) an impressive increase is observed resulting in an outstanding specific surface area of 3060 m^2 g^{-1} and an enormous micropore volume as high as 1.04 cm^3 g^{-1}. Simultaneously the total pore volume is slightly decreased to a value of 3.45 cm^3 g^{-1} being in accordance with the fact, that the pore system is now composed of micro- and small mesopores (**Table 2**, Figure 3b).[9]

The achieved high specific surface area of >3000 m^2 g^{-1}, a value which is usually only observed for highly activated carbons[38] or carbide-derived carbons (CDC),[39] evidences the impact of in situ activation. Mercury intrusion pore size distributions (Figure 3b) and TEM images (Figure 3c,d) confirm the almost perfect replication of the ZnO-NP shape and, thus, highlight the elegance of pore size tailoring. The relatively wide pore size distribution of HPCR prepared from Evonik Industries ZnO-NP (HPCR-EI) with a maximum at 40 nm is accompanied by the highest pore volume of all investigated samples (3.93 cm^3 g^{-1}).

The above mentioned flexibility of the presented approach allows the synthesis of highly porous carbon materials under precise manipulation of the pore size. Notable features are the hierarchical porous system with high meso/macropore volume as well as distinctive microporosity inside the carbon walls.

2.3. Structural Characterization of HPC/S Composite Based Cathodes

Since HPC offers not only outstanding total pore volumes ranging from 3.45 cm^3 g^{-1} (HPCR-SM) to 3.93 cm^3 g^{-1} (HPCR-EI) but also a hierarchical pore structure with tunable pore diameters and in situ generated microporosity with micropore volumes of 0.21 cm^3 g^{-1} (HPCW-USN) to 1.04 cm^3 g^{-1} (HPCR-SM) depending on the preparation procedure and ZnO-NP template used, this new class of carbon is excellently suited for the preparation of C/S composites by infiltration with sulfur and subsequent evaluation of performance determining parameters in Li-S battery tests.

As can be deduced from the SEM images showing the topography of characteristic cathode samples prepared from either

Table 2. Porosity of HPCR prepared from different ZnO-NP.

Template	Template specific surface area [m^2 g^{-1}]	HPCR specific surface area [m^2 g^{-1}]	HPCR total pore volume$^{a)}$ [cm^3 g^{-1}]	HPCR micropore volume$^{b)}$ [cm^3 g^{-1}]
US-Nano	14	1757	3.69	0.54
Evonik Industries	22	1632	3.93	0.51
Self-made	60	3060	3.45	1.04

[a)] calculated from the cumulated pore volume for pores with a diameter ≤ 400 nm using a combination of mercury intrusion data and nitrogen physisorption (micropore volume); [b)] calculated from the cumulated pore volume at a diameter of 2 nm pore size using the QSDFT method

HPCR-USN/S (Figure S7a) or HPCW-USN/S (Figure S7b) by roll-pressing, the cathode surface is smooth and flat, but not compacted. Despite several large pores penetrating into the active layer no cracks or evidence for delamination of small sized (<5 µm), homogeneously distributed composite particles is visible. The single composite particles are interwoven by a well distributed, percolating CNT network, which is anchored to their outer surface as is evidenced by the high resolution SEM images (Figure S7c,d). Accordingly, a highly porous, incompressible carbon backbone with persistent electron pathways is formed, that can withstand mechanical stress introduced by active material volume change during cycling. Sulfur agglomeration outside the porous carbon matrix is neither observed in the overview nor the high resolution SEM image of HPCR-USN/S (Figure S7a,c) evidencing that the infiltrated amount of sulfur (C/S ratio = 1:3, m:m) can be completely soaked up by a hierarchical pore system offering a sufficient micropore share. In contrast, the HPCW-USN/S composite particles exhibit a rather spherical and partially clumped together morphology as can be seen from the overview SEM image (Figure S7b). Whereas the HPCR-USN/S particles show a distinct surface roughness (Figure S7c), which is similar to that of the pristine HPCR-USN material (Figure S3c). The surface of the HPCW-USN/S composite in Figure S7d is smoother without the characteristic porous, bumpy features observed for the pristine HPCW-USN carbon (Figure S3d). This reduction of surface porosity points to the fact that homogeneous, complete infiltration of sulfur is not possible in the latter case and, thus, not simply a feature of the void total pore volume, which is approximately the same for both HPCW-USN (V_{total} = 3.81 $cm^3\,g^{-1}$) and HPCR-USN (V_{total} = 3.69 $cm^3\,g^{-1}$). It is rather driven by the share of micropores, which is much higher for the carbothermally reduced sample HPCR-USN (V_{micro} = 0.54 $cm^{-3}\,g^{-1}$) compared to the HCl-washed sample HPCW-USN (V_{micro} = 0.21 $cm^{-3}\,g^{-1}$). This finding is consistent with adsorption theory stating that micropores induce stronger capillary force than larger sized meso/macropores. Moreover, higher microporosity increases the available surface area in the carbon matrix, which most likely favors the formation of a homogenously distributed, thin sulfur film.

Interestingly, characteristic sulfur peaks [ICDD: 8-247] are observed in the XRD pattern of the C/S composites prepared from HPCW-USN as well as HPCR-USN (Figure S8a) indicating that sulfur does not exist in a completely amorphous state inside the pores of both carbon materials. However, this finding is still in agreement with the interpretation of the SEM images when considering that only about 0.43 (HPCW-USN/S) to 1.12 (HPCR-USN/S) gram of sulfur can be infiltrated in the micropores of 1 gram of the carbon host (**Figure 4**, assuming unhindered access and complete filling of all available micropores). Consequently, for the C/S (1:3, m:m) composite, a considerable share of 1.88 (HPCR-USN/S) to 2.57 (HPCW-USN/S) gram of sulfur per gram carbon is stored in large-sized meso/macropores (HPCR-USN: 70 nm; HPCW-USN: broad distribution between 40 and 200 nm), which obviously cannot suppress the nucleation of sulfur nanoparticles.

This particular behavior is further observed for the HPCR-EI/S composite having a sulfur distribution comparable to HPCR-USN/S (Figure 4), but a maximum at smaller pore diameter of 40 nm. However, since the pore size distribution is very broad the nucleation of sulfur nanoparticles is still not prevented leading to characteristic sulfur peaks in the XRD pattern of the HPCR-EI/S composite (Figure S8a). In contrast to HPCR-USN and HPCR-EI prepared from commercial ZnO-NP template, the HPCR-SM carbon prepared from ZnO-NP (SM) offered a sharp pore size distribution with maximum for 20 nm mesopores. This feature is further combined with the highest micropore share of all investigated samples (V_{micro} = 1.04 $cm^3\,g^{-1}$), which shifts the sulfur distribution to a high share of ca. 2.15 (HPCR-SM/S) gram of sulfur infiltrated in the micropores and only 0.85 gram of sulfur infiltrated in the mesopores of 1 gram of the carbon host (Figure 4). Consequently the nucleation of sulfur is effectively suppressed. The completely amorphous state of sulfur in HPCR-SM/S is further evidenced by the lack of characteristic sulfur peaks in the corresponding XRD pattern. The latter is also observed for the CMK-3/S reference sample (Figure S9), where the sulfur is besides the micropores completely infiltrated in small-sized mesopores (<5 nm) suppressing the formation of sulfur nanoparticles.

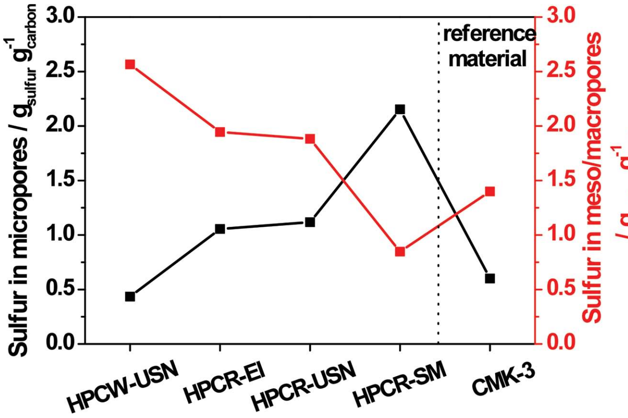

Figure 4. Theoretical sulfur distribution in micropores and meso/macropores, respectively, of different HPC/S composites with a sulfur-to-carbon ratio of 1:3 (1:2 for CMK-3). The calculation is based on the assumption that the complete micropore volume is filled with sulfur in the melt-infiltration step.

According to TG analysis under oxidative conditions (air atmosphere) the combustion of sulfur from the C/S composites took place at a temperature higher than 200 °C and was completed at a temperature of at most 425 °C (Figure S8b). The sulfur content in the as-prepared composites determined from this TG step were in almost perfect agreement with the adjusted carbon-to-sulfur ratio.

2.4. Electrochemical Performance of HPC/Sulfur Composites Based Cathodes

The structural motif, i.e., the pore geometry, of HPC is well suited to achieve a highly reversible, long-lasting electrochemical transformation of S_8 to Li_2S_2/Li_2S and vice versa via lithium polysulfides Li_2S_n ($8 \geq n \geq 4$) as soluble reaction intermediates. The main reason therefore is the presence of a hierarchical pore system combining high surface area micropores with spherical shaped meso/macropores, whose presence is illustrated in the

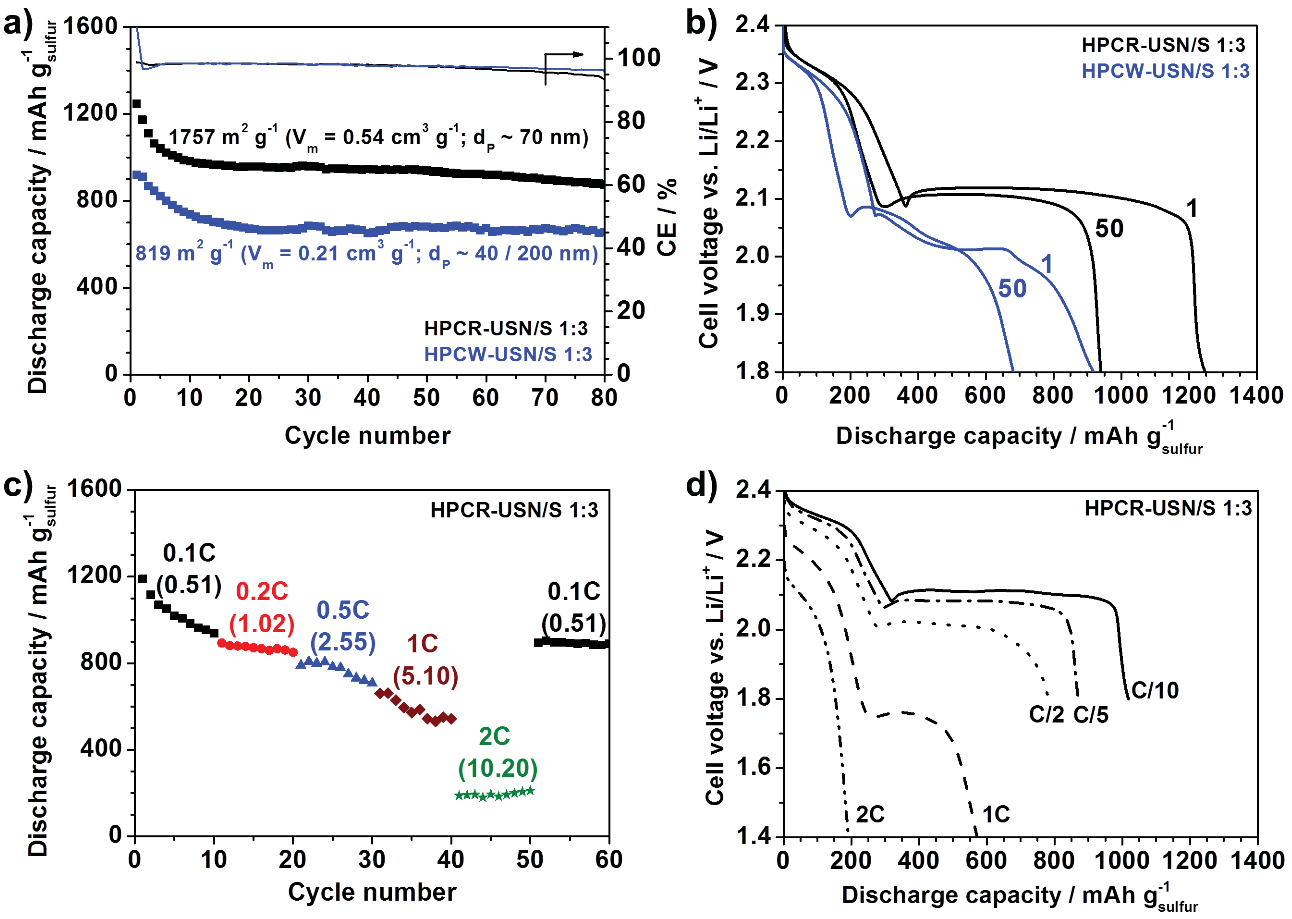

Figure 5. a) Comparison of cycling performance at C/10 (discharge capacity, cycling stability and Coulombic efficiency) for C/S composites containing HPC prepared via either HCl-washing or carbothermal reduction, b) 1st and 50th cycle discharge profiles of the samples depicted in a), c) Rate capability test (C/10–2C) of a sulfur cathode prepared from HPCR-USN/S composite. The values in brackets represent the corresponding current densities in mA cm^{-2}. d) Typical discharge voltage profiles of HPCR-USN/S composite at different rates (taken from each 5th cycle).

TEM images (Figure 2c (HPCR-USN), Figure 3c,d (HPCR-EI, HPCR-SM) and Figure S3e (HPCW-USN)). With regard to the comparability of the electrochemical results, it is highly important to note that all prepared carbon samples exhibit similar total pore volumes (see Table 1 and 2), although the size regime of the meso/macropores (20 nm to 200 nm) inside the carbon particles is largely different. Thus, when infiltrated in a fixed carbon-to-sulfur weight ratio of 1:3, the pore-filling degrees of the HPC/S composites are comparable and range from approx. 36.9 % (HPCR-EI/S) to 42.0 % (HPCR-SM/S). This leaves sufficient void space inside the composite particles for active material volume expansion and electrolyte uptake/storage. In contrast, the distribution between micropores and meso/macropores is largely different depending on both the ZnO-NP template used and the preparation process of HPC (W or R). This leads to variations in the specific surface area, which is directly proportional to the available micropore volume (Figure S10, Supporting Information). Moreover, the sulfur distribution between micro- and meso/macropores is shifted considerably as previously discussed (Figure 4). These specific conditions allow us to contribute to the scientific knowledge base by characterizing in more detail the influence of the pore structure of a carbon material, namely the meso/macropore size and SSA in HPC, on the electrochemical performance of the composite.

Considering that the single nanopores act as individual reaction chambers, the HPCR-USN structure offers superior properties compared to HPCW-USN. On the one hand, the active material (sulfur) can be soaked up inside the carbon particle more effectively, as was already described. On the other hand, fewer defects and cracks existing in the pore walls might help in preventing capacity loss due to polysulfide leakage. Even more important, the higher share of micropores located in the pore walls of carbothermally activated HPCR-USN introduces a high surface area of 1757 m^2 g^{-1} compared to 819 m^2 g^{-1} for HCl-washed HPCW-USN, which effectively triggers the homogeneous distribution of melt-infiltrated sulfur. During cycling the higher number of reaction sites not only improves the electrical contact to insulating S_8 and Li_2S_2/Li_2S precipitates, but also reduces the blocking of transport pores. The reason therefore is most likely the reduced share of sulfur located in meso/macropores clogging the interfaces between adjacent and spherical shaped pores. Accordingly, the penetration of electrolyte, i.e., Li-ions, is less hindered in HPCR-USN/S compared to HPCW-USN/S. This leads to an increase of the initial discharge capacity from 919 mAh g$^{-1}_{sulfur}$ (HPCW-USN/S) to 1246 mAh g$^{-1}_{sulfur}$ (**Figure 5**a). The stable discharge capacity is also increased from 656 mAh g$^{-1}_{sulfur}$ to 875 mAh g$^{-1}_{sulfur}$ (after

80 cycles at C/10) evidencing the superior pore characteristics of HPCR-USN for application in sulfur cathodes. Moreover, the discharge profiles of HPCR-USN/S and HPCW-USN/S (Figure 5b) show significant differences in their curvature. Whereas the high-voltage plateau shows the expected shape for both carbon materials, the low-voltage plateau of HPCW-USN/S is largely depressed due to polarization effects. Interestingly, this behavior is not changed after 50 cycles, indicating that it is not circumventable by formation of the cathode but rather associated deeply with the properties of the HPCW material, namely the lower surface area and the imperfect replication of the ZnO-NP template shape. In comparison, HPCR-USN/S exhibits the expected low-voltage plateau at approx. 2.1 V vs Li/Li$^+$ showing low polarization effects, because the numerous electrochemical reaction sites (micropores) surround the individual reaction chambers (meso/macropores). The advantage of this close contact is obvious. Even when the electrolyte is enriched with dissolved lithium polysulfides reaching its viscous maximum at the end of the high-voltage discharge plateau, the reaction sites are readily accessible for Li_2S/Li_2S_2 deposition due to the short diffusion distances. In consequence, the performance of the cell based on HPCR-USN/S is little affected by the electrolyte viscosity change during the discharge/charge process, even at high areal sulfur loadings ≥ 3 mg_{sulfur} cm^{-2}. This is further evidenced by the outstanding rate capability of HPCR-USN/S featuring discharge capacities as high as 661 mAh $g^{-1}{}_{sulfur}$ at a high current density of 5.1 mA cm^{-2} (1C) (Figure 5c).

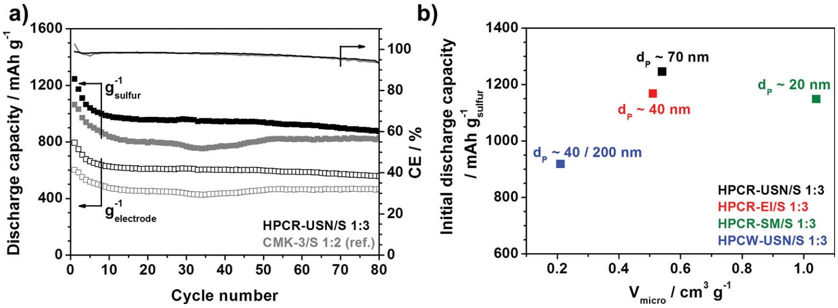

Figure 6. a) Cycling performance of the HPCR-USN/S sample compared to CMK-3/S (reference sample). b) Correlation between initial discharge capacity of the C/S composite cathodes at C/10 and micropore volume of the HPC prepared via HCl-washing and carbothermal reduction, respectively.

However, the discharge voltage profile (Figure 5d) is suppressed considerably in the low-voltage region due to sluggish reaction kinetics caused by deposition of insulating precipitates. Thus, at an even higher current density of 10.2 mA cm^{-2} (2C) solely the high-voltage plateau is preserved corresponding to a considerable reduced discharge capacity of not more than 211 mAh $g^{-1}{}_{sulfur}$. Nevertheless, when switching back to low discharge rates after application of high stress, i.e., high current densities, the initially extractable capacity can largely be recuperated.

The rate capability, with respect to the applicable current density, as well as the active material utilization of the HPCR-USN/S composite is far beyond previous publications in the field of porous carbons. For instance, the performance of a CMK-3/S composite, which was introduced by Nazar et al.[8] and is used as the reference system in this publication (**Figure 6**a), was surpassed by more than 160 mAh $g^{-1}{}_{sulfur}$ (comparison of the first 20 cycles in agreement with the cited publication). Although other mainly mesoporous carbons applied in C/S composites showed higher initial sulfur utilization of 60–75 % (1000–1250 mAh $g^{-1}{}_{sulfur}$) being close to HPCR-USN/S, the adjusted sulfur content was rather low and faster capacity fading (32–50% within not more than 100 cycles) was observed.[21,40,41] This was largely attributed to the reduced carbon-sulfur contact in mesopores carbons which is in good agreement with our findings concerning the performance of the mainly meso/macroporous HPCW-USN/S composite. Consequently, also hierarchical micro/mesoporous carbons were studied. Although good performance (1000–1300 mAh $g^{-1}{}_{sulfur}$) at moderate current densities (0.25–1.67 mA cm^{-2}) was shown, the adjusted sulfur content was rather low to assure the sole impregnation of micropores and, thus, avoid blocking of the mesopores.[22–25] However, this inevitably led to insufficient capacities per electrode weight. This is why our investigations, in contrast to these previous reports, were performed under rather realistic conditions meaning that both the sulfur loading and sulfur content were high to address the “two lows”,[42,43] whereas the amount of electrolyte used was low to reduce its weight share. Unfortunately, both HPCR-USN/S and HPCRW-USN/S composite still suffer active material loss due to polysulfide leakage as is evidenced by the initial capacity drop (Figure 5a). This is most likely caused by the wide-open porosity introduced by the large-sized meso/macropores (40 nm to 200 nm) and the insufficient surface area (microporosity) provided by the carbon host, respectively.

To analyze this in more detail, we used sulfur-infiltrated HPCR prepared from different ZnO-NP templates, namely HPCR-EI/S and HPCR-SM/S, and compared the results to HPCR-USN/S. Interestingly, the correlation between initial discharge capacity and micropore volume (Figure 6b) observed for HPCW-USN/S (d_P ≈ 40/200 nm) and HPCR-USN/S (d_P ≈ 70 nm) does also account for HPCR-EI/S (d_P ≈ 40 nm) meaning that an increase in available surface area does improve the sulfur utilization. This is again explainable by a more homogenous sulfur distribution inside the carbon matrix, which reduces pore blocking, and a higher number of electrochemical reaction sites. Evidence is provided by the discharge capacity characteristics and the discharge voltage profiles, respectively (**Figure 7**a,b). The low-voltage plateau of HPCR-EI/S (2.11 V vs Li/Li$^+$) is slightly depressed compared to HPCR-USN/S (2.12 V vs Li/Li$^+$) and the initial as well as stable discharge capacity (after 80 cycles) is reduced from 1246 mAh $g^{-1}{}_{sulfur}$ and 875 mAh $g^{-1}{}_{sulfur}$ (HPCR-USN/S) to 1168 mAh $g^{-1}{}_{sulfur}$ and 820 mAh $g^{-1}{}_{sulfur}$ (HPCR-EI/S), respectively. However, the smaller meso/macropores in HPCR-EI are, most likely, beneficial for the cycling stability as can be deduced from the more stable capacity plateau (Figure 7a). Between cycle 20 and 80 a degradation of only 4.43 % is observed for HPCR-EI/S compared to 8.66 % for HPCR-USN/S. The further reduction of mesopore size to approx. 20 nm in HPCR-SM

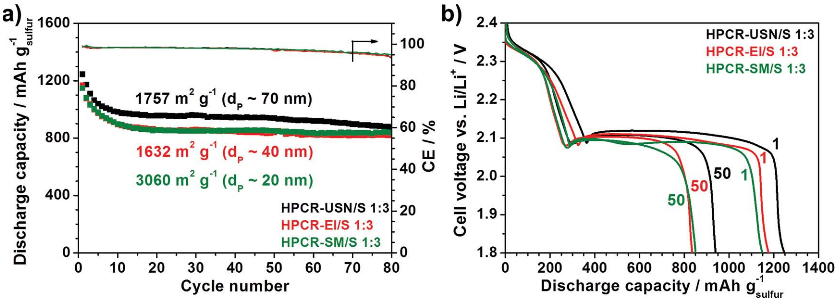

Figure 7. a) Comparison of cycling performance at C/10 (discharge capacity, cycling stability and Coulombic efficiency) for C/S composites containing HPC prepared from different ZnO-NP templates (USN, EI, SM), b) 1st and 50th cycle discharge profiles of the samples depicted in (a).

was accompanied by a significant increase in specific surface area to a value as high as 3060 m^2 g^{-1}. Interestingly, the correlation depicted in Figure 6b becomes invalid for HPCR-SM/S meaning that the increase in micropore volume, i.e., specific surface area, led to a reduction in initial discharge capacity to 1149 mAh g$^{-1}_{sulfur}$. Moreover, the stable discharge capacity of HCPR-SM/S is only at about 839 mAh g$^{-1}_{sulfur}$. Both values are largely comparable to the HPCR-EI/S composite, although the HPCR-EI carbon only offers about half the surface area of HPCR-SM. This unexpected, detrimental behavior is largely attributable to the reduction in meso/macropore size from ca. 40 nm (HPCR-EI) to ca. 20 nm (HPCR-SM) increasing the thread of pore blocking during melt-infiltration and cycling, which restrains the transport of Li-ions as well as polysulfides to the reaction sites. This is evidenced by the discharge voltage profiles of HPCR-SM/S (Figure 7b), showing increased polarization in the low-voltage plateau (2.09 V vs Li/Li$^+$) compared to HPCR-USN/S and HPCR-EI/S.

However, both the potential of the low-voltage plateau and the length of the high-voltage plateau remain nearly unchanged for HPCR-SM/S, which indicates that the small sized mesopores ($d_P \approx 20$ nm) combined with a high micropore share (high surface area) can improve the cycling stability. Hence, the capacity decay of 2.10 % observed for HPCR-SM/S between cycle 20 and 80 is the lowest of all investigated hierarchical porous carbons prepared by carbothermal reduction (HPCR).

3. Conclusion

We have presented a novel pathway for the efficient as well as scalable synthesis of hierarchical porous carbons with tailored porosity without any need of toxic or reactive gases. Impressively, the carbothermal reduction process, furthermore, facilitates the access of a hierarchical pore system with distinctive microporosity inside the thin carbon walls leading to very high specific surface areas even exceeding 3000 m^{-2} g^{-1}. Adjusting the ZnO-NP template size, HPC with internal pore volumes as high as 3.9 cm^3 g^{-1} and tailored pore sizes reaching from 20 nm to 200 nm with ideal template replication are obtained. The synergetic advantage of that bimodal porosity renders them particularly suitable for the application in high energy density lithium-sulfur batteries. A high capacity of > 1200 mAh g^{-1} sulfur (> 750 mAh g^{-1} electrode) at a high sulfur loading of ≥3 mg cm^{-2} was achieved as well as the highest ever reported rate capability, with respect to realistic applied oriented conditions meaning that both the sulfur loading and sulfur content are high to maintain the advantageous properties of the lithium-sulfur battery. Moreover, the novel carbons are promising high performance adsorbents for enzyme applications, cytokine removal and mass transport limited catalytic applications.

4. Experimental Section

Synthesis of HPCR: In a typical procedure 6 g of ZnO nanoparticles (purchased from US Research Nanomaterials Inc. (US-Nano (USN), product specification 10–30 nm) and provided from Evonik Industries (EI, product name VP ZnO 20) as well as self-made ZnO nanopaticles (SM)) were thoroughly mixed in a glass Petri dish with 10 ml aqueous solution consisting of 5.25 g sucrose (Sigma Aldrich; ≥ 99%) and 100 mg of a 2.5 M aqueous sodium hydroxide solution (Carl Roth, ≥ 99%). The white dispersion was placed in a furnace for 3 h at 100 °C and subsequently further 6 h at 160 °C. The carbothermal reduction was carried out in a horizontal tubular furnace with an argon flow of 1 slm (standard liter per minute) by a heating rate of 5 K min^{-1} to 950 °C and tempered there for 2 h.

Synthesis of HPCW: To avoid carbothermal reduction a marginal variation of the above described instruction was carried out. The 10 ml aqueous solution contains 3 g sucrose (Sigma Aldrich; ≥ 99%) and 80 mg of sulfuric acid (Sigma Aldrich; 96% in water). Furthermore, the pyrolysis temperature was decreased to 800 °C to avoid a carbothermal reduction. The C/ZnO composite obtained after pyrolysis was washed with 1 M HCl solution for 2 hours to remove the ZnO template. The template-free carbon was filtered, washed three times with distilled water and finally dried over night at 80 °C. CMK-3 reference material was prepared as reported elsewhere.[44]

ZnO Nanoparticle Synthesis: ZnO nanoparticles were produced in house using a flame spray pyrolysis process (FSP) as introduced by Mädler et al.[45] A 0.5 M solution of zinc acrylate dissolved in a 94:6 mixture of methanol and acetic acid was fed with 2 ml min^{-1} through a commercial nozzle (NPS10, Tethis) and ignited by a surrounding supporting-flame to prevent the main flame from self-extinguishing. The supporting-flame gas flow consisted of 1.58 slm CH_4 and 1.50 slm O_2. The liquid feed was delivered by a micro annular gear pump (mzr-2905, HNP Mikrosysteme GmbH) and dispersed by 3.85 slm O_2 with a dispersion gas pressure drop of 2.0 bar adjusted by a displaceable annular gap encircling the liquid feed capillary. Additionally a sheath gas flow of 5 slm O_2 was supplied through a porous metal ring to ensure full combustion of the precursor solution. All gas flows were controlled by thermal mass flow controllers (Bronkhorst). The synthesized particles were collected on a binder free glass fiber filter (GF/A Whatman) with the help of a rotary vane pump (Vacuubrand RZ 9).

Composite Preparation: The preparation of the C/S composite was carried out via melt-infiltration of sulfur. The C/S composite was prepared by thoroughly mixing of the porous carbon material (HPCW or HPCR) and pristine sulfur (Sigma Aldrich, ≥ 99.5 %) in a porcelain mortar. The weight ratio of carbon-to-sulfur was adjusted to 1:3 for all HPCR and HPCW (1:2 for CMK-3 reference). The homogenous powder was subsequently transferred into a porcelain crucible and heated to 155 °C for 12 h under air to induce the uptake of molten sulfur in the pores of the carbon material by capillary force.

Electrode Preparation: Cathodes were prepared from the C/S composites following a solvent-free roll-press procedure reported elsewhere.[10] However, the cathode composition (weight ratio of C/S composite : multi-walled carbon nanotube conductive additive : PTFE binder) was slightly changed to 85 : 12 : 3, thus not only reducing the amount of inactive components but also improving the wettability (porosity) of the active material film. The punched circular electrodes had a diameter of 12 mm with a typical active material loading of 3.00–4.85 mg_{sulfur} cm^{-2}.

Structural Characterization: The thermal analysis was carried out with a Netzsch STA 409 PC LUXX with a heating rate of 5 K/min under inert conditions (Ar)) and under oxidizing conditions (synthetic air), respectively. The morphology of the samples was characterized by Scanning Electron Microscopy (SEM) on a Stereoscan 260 SEM as well as by Transmission Electron Microscopy (TEM) on a JEOL JEM-2100. Powder X-ray diffraction patterns were collected on a Stoe Stadi-P (Cu-$K\alpha_1$ radiation). Nitrogen physisorption measurements at 77 K were performed on a Quantachrome Quadrasorb after degassing of the samples overnight under vacuum at 150 °C. Multi-point BET equation in the rage of 0.05 to 0.20 relative pressures p/p_0 was used to determine the specific surface area. The micropore volumes were calculated from the cumulative pore volumes at a pore diameter of 2 nm using the Quenched Solid Density Functional Theory (QSDFT) calculation for carbon (slit/cylindrical pores, adsorption branch kernel). The meso/macropore volumes (5 nm to 400 nm) as well as the pore size distributions were determined by Mercury intrusion porosimetry using AutoPore IV 9500 V1.07 according to ISO 15901-1 instruction.

Electrochemical Characterization: Lithium-sulfur half cells were prepared by stacking the C/S composite cathode (working electrode), a porous polypropylene separator (Celgard 2500) and elemental lithium (counter and reference electrode) in CR2016 coin cells. Before sealing an appropriate amount of electrolyte (6.8 µl mg^{-1}_{sulfur} 1M LiTFSI and 0.25M $LiNO_3$ in DME/DOL (1:1 by volume)) was added. The work was carried out under inert atmosphere in an argon filled glove box (< 0.1 ppm O_2 and < 0.1 ppm H_2O) to avoid contamination. The capacity and long-term stability of the Li-S cells comprising the C/S composite cathodes was characterized by galvanostatic cycling with a BASYTEC CTS cell test system. Typically the cells were operated at a constant rate of C/10 (1C = 1672 mA g^{-1}_{sulfur}) in a voltage range of 1.8 – 2.6 V vs Li/Li^+. However, also rate capability tests (discharge // charge rate: C/10 // C/10; C/5 // C/5; C/2 // C/5; 1C // C/5; 2C // C/5) were preformed, whereas the voltage window was readjusted to 1.4 – 2.6 V vs Li/Li^+ at high discharge rates (1C – 2C) to account for the increased polarization of the cathode.

Supporting Information

Supporting Information is available from the Wiley Online Library or from the author.

Acknowledgement

This work was financially supported by the German ministry of Education and Science (BMBF) through the project "Nanomaterials for future generation Lithium-Sulfur-batteries" (MaLiSu).

Received: August 13, 2014
Revised: October 20, 2014

---

[1] P. G. Bruce, S. A. Freunberger, L. J. Hardwick, J.-M. Tarascon, *Nat. Mater.* **2012**, *11*, 19.
[2] X. Ji, L. F. Nazar, *J. Mater. Chem.* **2010**, *20*, 9821.
[3] H. D. Yoo, E. Markevich, G. Salitra, D. Sharon, D. Aurbach, *Mater. Today* **2014**, *17*, 110.
[4] Z. Wei Seh, W. Li, J. J. Cha, G. Zheng, Y. Yang, M. T. McDowell, P.-C. Hsu, Y. Cui, *Nat. Commun.* **2013**, *4*, 1331.
[5] R. Elazari, G. Salitra, Y. Talyosef, J. Grinblat, C. Scordilis-Kelley, A. Xiao, J. Affinito, D. Aurbach, *J. Electrochem. Soc.* **2010**, *157*, A1131.
[6] X. He, J. Ren, L. Wang, W. Pu, C. Jiang, C. Wan, *J. Power Sources* **2009**, *190*, 154.
[7] Y. V. Mikhaylik, J. R. Akridge, *J. Electrochem. Soc.* **2004**, *151*, A1969.
[8] X. Ji, K. T. Lee, L. F. Nazar, *Nat. Mater.* **2009**, *8*, 500.
[9] M. Oschatz, S. Thieme, L. Borchardt, M. R. Lohe, T. Biemelt, J. Brückner, H. Althues, S. Kaskel, *Chem. Commun.* **2013**, *49*, 5832.
[10] S. Thieme, J. Brückner, I. Bauer, M. Oschatz, L. Borchardt, H. Althues, S. Kaskel, *J. Mater. Chem. A* **2013**, *1*, 9225.
[11] N. Jayaprakash, J. Shen, S. S. Moganty, A. Corona, L. A. Archer, *Angew. Chem. Int. Ed.* **2011**, *50*, 5904.
[12] G. He, S. Evers, X. Liang, M. Cuisinier, A. Garsuch, L. F. Nazar, *ACS Nano* **2013**, *7*, 10920.
[13] L. Ji, M. Rao, H. Zheng, L. Zhang, Y. Li, W. Duan, J. Guo, E. J. Cairns, Y. Zhang, *J. Am. Chem. Soc.* **2011**, *133*, 18522.
[14] N. Li, M. Zheng, H. Lu, Z. Hu, C. Shen, X. Chang, G. Ji, J. Cao, Y. Shi, *Chem. Commun.* **2012**, *48*, 4106.
[15] G. Zhou, D.-W. Wang, F. Li, P.-X. Hou, L. Yin, C. Liu, G. Q. Lu, I. R. Gentle, H.-M. Cheng, *Energy Environ. Sci.* **2012**, *5*, 8901.
[16] S. Dörfler, M. Hagen, H. Althues, J. Tübke, S. Kaskel, M. J. Hoffmann, *Chem. Commun.* **2012**, *48*, 4097.
[17] J. Brückner, S. Thieme, H. T. Grossmann, S. Dörfler, H. Althues, S. Kaskel, *J. Power Sources* **2014**.
[18] L. Yuan, H. Yuan, X. Qiu, L. Chen, W. Zhu, *J. Power Sources* **2009**, *189*, 1141.
[19] J.-j. Chen, Q. Zhang, Y.-n. Shi, L.-l. Qin, Y. Cao, M.-s. Zheng, Q.-f. Dong, *Phys. Chem. Chem. Phys.* **2012**, *14*, 5376.
[20] S. Evers, L. F. Nazar, *Acc. Chem. Res.* **2013**, *46*, 1135.
[21] X. Li, Y. Cao, W. Qi, L. V. Saraf, J. Xiao, Z. Nie, J. Mietek, J.-G. Zhang, B. Schwenzer, J. Liu, *J. Mater. Chem.* **2011**, *21*, 16603.
[22] C. Liang, N. J. Dudney, J. Y. Howe, *Chem. Mater.* **2009**, *21*, 4724.
[23] G. He, X. Ji, L. Nazar, *Energy Environ. Sci.* **2011**, *4*, 2878.
[24] J. Schuster, G. He, B. Mandlmeier, T. Yim, K. T. Lee, T. Bein, L. F. Nazar, *Angew. Chem. Int. Ed.* **2012**, *51*, 3591.
[25] G. Xu, B. Ding, P. Nie, L. Shen, H. Dou, X. Zhang, *ACS Appl. Mater. Interfaces* **2014**, *6*, 194.
[26] J. T. Lee, Y. Zhao, S. Thieme, H. Kim, M. Oschatz, L. Borchardt, A. Magasinski, W. I. Cho, S. Kaskel, G. Yushin, *Adv. Mater.* **2013**, *25*, 4573.
[27] M. Oschatz, L. Borchardt, K. Pinkert, S. Thieme, M. R. Lohe, C. Hoffmann, M. Benusch, F. M. Wisser, C. Ziegler, L. Giebeler, M. H. Rümmeli, J. Eckert, A. Eychmüller, S. Kaskel, *Adv. Energy Mater.* **2014**, *4*, 1300645.
[28] Y. Meng, D. Gu, F. Zhang, Y. Shi, H. Yang, Z. Li, C. Yu, B. Tu, D. Zhao, *Angew. Chem. Int. Ed.* **2005**, *44*, 7053.
[29] N. Fechler, T.-P. Fellinger, M. Antonietti, *Adv. Mater.* **2013**, *25*, 75.
[30] M. Mecklenburg, A. Schuchardt, Y. K. Mishra, S. Kaps, R. Adelung, A. Lotnyk, L. Kienle, K. Schulte, *Adv. Mater.* **2012**, *24*, 3486.
[31] P. Mbuyisa, S. P. Bhardwaj, F. Rigoni, E. Carlino, S. Pagliara, L. Sangaletti, A. Goldoni, M. Ndwandwe, C. Cepek, *Carbon* **2012**, *50*, 5472.
[32] R. Ryoo, S. H. Joo, S. Jun, *J. Phys. Chem. B* **1999**, *103*, 7743.
[33] S.-W. Bian, I. A. Mudunkotuwa, T. Rupasinghe, V. H. Grassian, *Langmuir* **2011**, *27*, 6059.
[34] M. L. Kahn, M. Monge, V. Collière, F. Senocq, A. Maisonnat, B. Chaudret, *Adv. Funct. Mater.* **2005**, *15*, 458.
[35] L. Yang, Z. Zhang, Z. Wang, Y. Sun, M. Gao, J. Yang, Y. Yan, *Physica E* **2013**, *54*, 53.
[36] U. Özgür, Y. I. Alivov, C. Liu, A. Teke, M. A. Reshchikov, S. Doğan, V. Avrutin, S.-J. Cho, H. Morkoç, *J. Appl. Phys.* **2005**, *98*, 41301.
[37] S. Polarz, A. V. Orlov, F. Schüth, A.-H. Lu, *Chem. Eur. J.* **2007**, *13*, 592.
[38] M. Oschatz, L. Borchardt, I. Senkovska, N. Klein, M. Leistner, S. Kaskel, *Carbon* **2013**, *56*, 139.
[39] M. Rose, E. Kockrick, I. Senkovska, S. Kaskel, *Carbon* **2010**, *48*, 403.

[40] C. Zhang, H. B. Wu, C. Yuan, Z. Guo, X. W. D. Lou, *Angew. Chem. Int. Ed.* **2012**, *51*, 9592.

[41] J. Zheng, M. Gu, M. J. Wagner, K. A. Hays, X. Li, P. Zuo, C. Wang, J.-G. Zhang, J. Liu, J. Xiao, *J. Electrochem. Soc.* **2013**, *160*, A1624.

[42] M. Wang, W. Wang, A. Wang, K. Yuan, L. Miao, X. Zhang, Y. Huang, Z. Yu, J. Qiu, *Chem. Commun.* **2013**, *49*, 10263.

[43] L.-X. Miao, W.-K. Wang, A.-B. Wang, K.-G. Yuan, Y.-S. Yang, *J. Mater. Chem. A* **2013**, *1*, 11659.

[44] L. Borchardt, M. Oschatz, S. Paasch, S. Kaskel, E. Brunner, *Phys. Chem. Chem. Phys.* **2013**, *15*, 15177.

[45] L. Mädler, H. Kammler, R. Mueller, S. Pratsinis, *J. Aerosol. Sci.* **2002**, *33*, 369.